ARTICLE

OPEN

Check for updates

Interrogating helical nanorod self-assembly with fractionated cellulose nanocrystal suspensions

Camila Honorato-Rios [1] & Jan P. F. Lagerwall[1✉]

The helical self-assembly of cholesteric liquid crystals is a powerful motif in nature, enabling exceptional performance in many biological composites. Attempts to mimic these remarkable materials by drying cholesteric colloidal nanorod suspensions often yield films with a non-uniform mosaic-like character, severely degrading optical and mechanical properties. Here we show—using the example of cellulose nanocrystals—that these problems are due to rod length dispersity: uncontrolled phase separation results from a divergence in viscosity for short rods, and variations in pitch can be traced back to a twisting power that scales with rod length. We present a generic, robust and scalable method for fractionating nanorod suspensions, allowing us to interrogate key aspects of cholesteric self-assembly that were previously hidden by colloid dispersity. By controlled drying of fractionated suspensions, we can obtain mosaic-free films that are uniform in colour. Our findings unify conflicting observations and open routes to biomimetic artificial materials with performance that can compete with that of nature's originals.

[1] Department of Physics & Materials Science, University of Luxembourg, 1511 Luxembourg, Luxembourg. ✉email: jan.lagerwall@lcsoftmatter.com

I n a colloidal cholesteric (chiral nematic) liquid crystal phase[1], the nanorods align in a direction **n** (the director) that is helically modulated along an axis **m⊥n**. Iridescent reflection, circularly polarised with the same handedness as the helix, arises in a narrow wavelength band if the helix pitch p is on the order of visible light wavelengths[2]. This structural colour is defined by the cholesteric version of Bragg's law:

$$\lambda = \bar{n}p\cos\theta, \qquad (1)$$

where λ is the wavelength in air, $\bar{n}$ is the average cholesteric refractive index and θ is the incidence angle to **m**. Cholesteric Bragg reflection can be seen in the strikingly coloured and circularly polarised reflections from cuticles of certain beetles[3,4], and even from some fruits[5,6], revealing their helical arrangement of fibres of chitin and cellulose, respectively. In fact, cholesteric helical self-assembly can be found across a large range of biomaterials[7], providing advantages beyond optics for, e.g., optimised packing of DNA/RNA[8–10] and spectacular mechanical properties of composites built around collagen[11,12], amyloid[13], chitin[14,15] or cellulose[16,17]. Attempts to mimic this structuring via self-assembly in cholesteric colloidal nanorod suspensions, for instance by drying cholesteric suspensions of cellulose nanocrystals (CNCs)[18], often yield non-uniform films reflecting a range of colours with imperfect circular polarisation, and reproducibility and tunability are challenging[1,19–24].

We show in this study that these problems can be resolved by reducing the dispersity of CNC suspensions by fractionation. At the same time, the availability of CNC suspensions with low dispersity shines new light on intriguing fundamental questions of colloidal cholesteric self-assembly. Our fractionation method is based on the classic Onsager theory for explaining the spontaneous appearance of nematic long-range orientational order in non-disperse colloidal nanorod suspensions[25], stating that the isotropic phase becomes unstable beyond a rod volume concentration $\phi = \phi_0 = 3.3d/L$, where d and L are the diameter and length, respectively, of the rods (the theory assumes cylindrical rods). Liquid crystalline nuclei—tactoids[1]—then separate out, with a larger $\phi = \phi_1 = 4.5d/L$, the lower stability limit of the anisotropic nematic phase. For a chiral system, like the CNC suspensions in this study, the anisotropic phase is chiral nematic, or cholesteric.

The dependence of ϕ_0 and ϕ_1 on rod aspect ratio means that the separation between anisotropic and isotropic phases in a disperse system, with varying rod aspect ratios, can be used to separate long from short rods. The principle was demonstrated for carbon nanotubes[26] and for CNCs[27] and we recently applied it systematically to separate out the longest and shortest CNCs, respectively, from pristine suspensions[28]. Here we introduce, based on the same principle, a new fractionation methodology that is scalable to large volumes, and we also present a new scheme that partitions all CNCs in a pristine suspension into separate fractions with stepwise varying average length.

With access to these fractions, we can also identify a helical twisting power (HTP), inspired by the corresponding concept in thermotropic cholesterics but with somewhat different interpretation in this case of a colloidal cholesteric. We find that this key parameter, determining the equilibrium helix pitch p_0 at a certain CNC concentration, increases with rod length. This contrasts with theoretical predictions and preliminary experimental studies. Moreover, we demonstrate that the liquid crystal self-assembly dynamics changes strongly between fractions, slowing to a halt in suspensions with the shortest CNCs.

Results and discussion

Fractionation of cellulose nanocrystals. Because they are difficult to determine experimentally[1], we generally do not work with the CNC volume concentrations ϕ_0 and ϕ_1, instead using the corresponding critical mass concentrations w_0 and w_1. With $w_1 > w_0$ the anisotropic phase is denser than the isotropic, hence tactoids sink by gravity in the biphasic regime, $w_0 < W < w_1$, where W is the global CNC mass concentration of the sample. If a biphasic sample is left undisturbed, the anisotropic phase will form a bulk sediment distinct from the isotropic supernatant, see Fig. 1d, e. We exploit this phase separation by filling the pristine CNC suspension (general characterisation in Supplementary Note 1), inherently highly disperse in length[1,17,21], into a separatory funnel from which we can easily extract the sedimented anisotropic phase after 1–2 weeks. Significantly, a spontaneous fractionation of CNCs accompanies the phase separation[26–28]. This can be explained by the dependence on the critical mass concentrations on aspect ratio. In a simplified picture, adequate for the scope of this paper, the decrease in w_0 with increasing L/d means that the first anisotropic phase to nucleate upon concentrating a disperse isotropic suspension contains the longest CNCs (concerning d, see Supplementary Note 2), resulting in their physical segregation.

We call our initial biphasic suspensions $init_{20}$ and $init_{50}$, with W selected to yield volume fractions of anisotropic phase $\Phi = 20\%$ and $\Phi = 50\%$, respectively. While the latter builds on our previously published method[28], $init_{20}$ is the start of a new scheme. Both schemes are illustrated graphically in Fig. 1a, b, and full details are given in the 'Methods' section and Supplementary Note 3. The total mass of CNC suspension in our funnels is 800 g, limited by the size of the funnel. With larger funnels, the fractionation method can easily be scaled up.

The 20% anisotropic sediment in the 20/80 scheme (we call this fraction a_{20}, see Fig. 1a) contains the CNCs with highest L, with efficient fractionation already after a single step, see Fig. 1c. The average length $\bar{L}$ increases by 41% from $\bar{L}$ @$init_{20} = 0.195\,\mu m$ to $\bar{L}$@$a_{20} = 0.275\,\mu m$ and the dispersity (defined and discussed in Supplementary Note 2) decreases by 39% from ς@$init_{20} = 0.28$ to ς@$a_{20} = 0.17$ (see Table 1 and Supplementary Fig. 5). We repeat the procedure with the 80% isotropic supernatant (i_{80}, see Fig. 1a), first concentrating it until also this fraction produces 20/80 separation in the separatory funnel. In the new sediment (being the 20% anisotropic fraction of the first 80% isotropic fraction, we call it $i_{80}a_{20}$, see Fig. 1a) we get the second longest set of CNCs, $\bar{L}$ decreasing correspondingly in the new supernatant, which we label i_{80}^2 (twice in a row we extract the 80% isotropic fraction, Fig. 1a). We repeat the procedure twice further, giving us $i_{80}^2a_{20}$ and $i_{80}^3a_{20}$ from each anisotropic sediment as well as i_{80}^3 and i_{80}^4 from the isotropic supernatants.

While the 20/80 scheme yields the longest CNC fraction in the first step and the shortest CNC fraction in the last step (Fig. 1a), the 50/50 scheme produces its two extreme fractions at the end (Fig. 1b). The equal volumes of isotropic and anisotropic phases in the $init_{50}$ sample are separated physically and then the isotropic fraction is concentrated, while the anisotropic fraction is diluted until both new fractions show 50/50 phase separation in separatory funnels. As illustrated in Fig. 1b, the separation, concentration and dilution are repeated multiple times, each time discarding the new isotropic fraction arising from an anisotropic starting fraction, and vice versa. We collect generations 3–5 of the anisotropic fractions for investigation, calling them a_{50}^3, a_{50}^4 and a_{50}^5, and generations 3–4 of the isotropic fractions, consequently labelled i_{50}^3 and i_{50}^4.

Behaviour in the biphasic regime of each fraction. For each fraction, we prepare samples at $W = 1–12$ wt.% (Supplementary
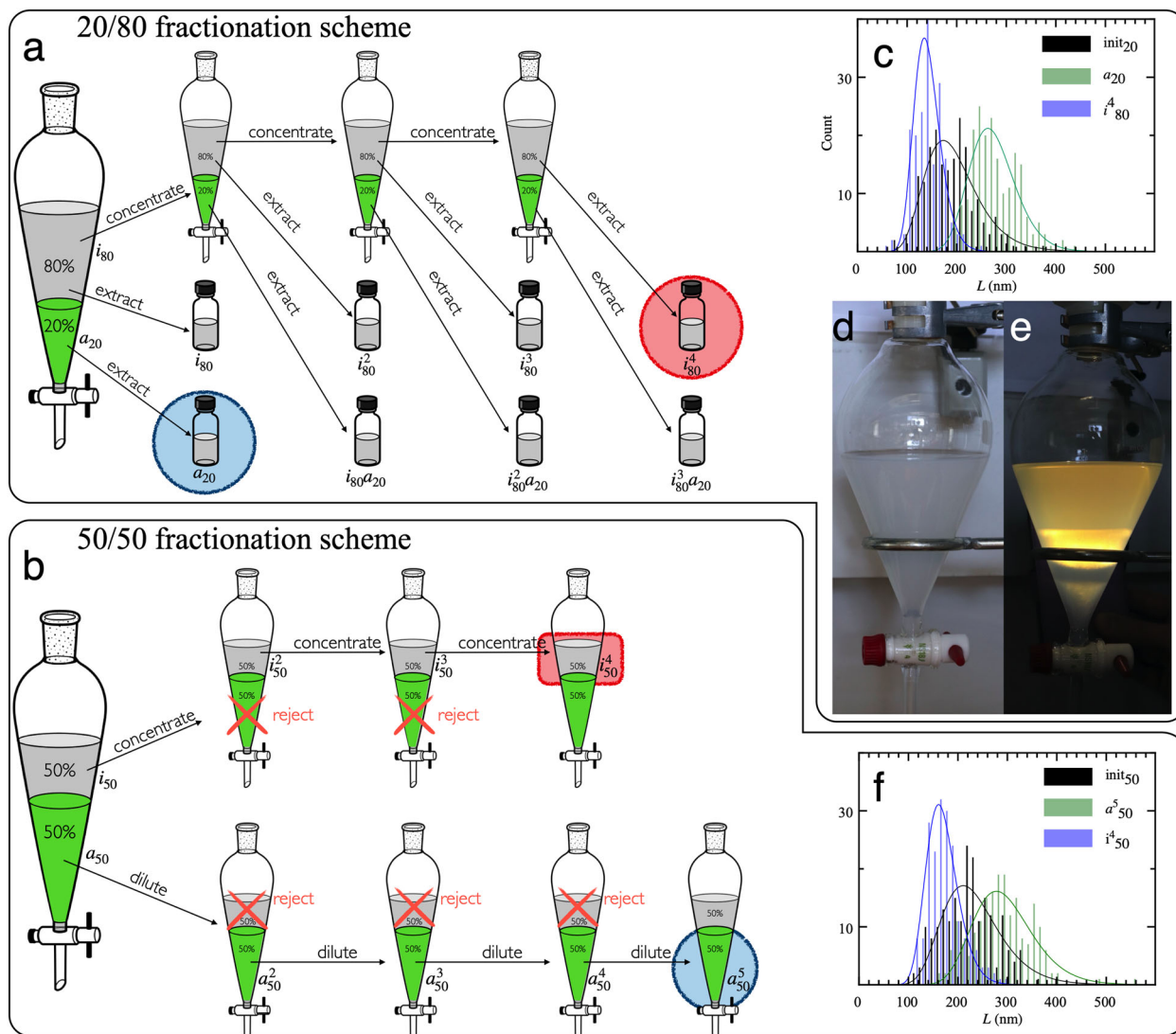
Fig. 1 Fractionation of CNCs by liquid crystal formation. The different steps in the two schemes, as well as the labelling of each fraction, are summarised for 20/80 separation in (**a**) and 50/50 separation in (**b**). For each scheme, the longest CNC fraction is highlighted with blue background and the shortest CNC fraction with red background. Excerpts (initial suspension and the two extreme fractions from each scheme) of the resulting distributions of CNC lengths L are shown in (**c**) and (**f**). Bars are raw data from AFM analysis, curves are log-normal fits to experimental data. All data are summarised in Table 1 and Supplementary Fig. 5, and the analysis procedure is described in Supplementary Note 2. The boundary between isotropic and cholesteric phases is difficult to see with ambient light (**d**) but it is revealed by illumination from behind (**e**).

Figs. 6 and 7), allowing us to establish the respective phase separation diagrams, see Fig. 2. By fitting a linear function (see 'Methods') to the data we extract w_0 and w_1 for each fraction as fitting parameters (Table 1). With the possible exception of the high-generation isotropic fractions of the 50/50 scheme, for which w_1 cannot be established reliably (explained below), the width of the biphasic regime, $\Delta w = w_1 - w_0$, is significantly reduced compared to either initial suspension, indicating a reduced dispersity in length. The effect is greatest for the long-CNC fractions, $\Delta w @ a_{20} = 1.8\%$ and $\Delta w @ a_{50}^5 = 1.5\%$ about three times smaller than Δw of the respective initial suspensions.

There is a striking difference between the fractionation of the two schemes, immediately clear by comparing Fig. 2a, b. With the 20/80 scheme, w_0 and w_1 move stepwise (about 2 wt.% step size) to higher CNC content for each new generation of fractionation. In contrast, the 50/50 scheme immediately locates each branch at extreme ends of the diagram, pushing a_{50}^n fractions to increasingly

reduced w_0 and w_1 with each new generation n, whereas w_0 in i_{50}^n fractions increases steadily.

Biphasic suspensions ($w_0 < W < w_1$) of fractions with long CNCs show rapid phase separation along gravity, reaching their final equilibrium state in about a day (Fig. 3a, left; Supplementary Movie 1 and Supplementary Note 5). In strong contrast, suspensions of short CNCs have not reached their equilibrium separation even after 3 months (Fig. 3a, right; Supplementary Movie 2 and Supplementary Note 5). This very significant difference in time to reach equilibrium has enormous impact on research on as well as applications of CNCs. The very slow sedimentation of tactoids with $w_1 \gtrsim 7\%$ means that accurate establishment of the phase separation diagram is practically impossible for short CNCs, as even 18 months of waiting is not enough to fully separate the phases (Supplementary Fig. 9). Hence, $\Phi(W)$ is easily underestimated for pristine suspensions that contain many short CNCs. The impact grows with CNC

Table 1 Characteristics of the two initial CNC suspensions used in the study and all fractions obtained following the 20/80 and 50/50 fractionation procedures.

Fraction	w_0 (%)	w_1 (%)	Δw (%)	4.5/3.3w_0 (%)	$w_1(p_0)$ (%)	HTP ($\mu m^{-1}\%^{-1}$)	$\bar{L}$ (nm)	ς	$\bar{\imath}$ (nm)	L_{min} (nm)	L_{max} (nm)	$\bar{d}_{AFM}$ (nm)	$\bar{L}/\bar{d}_{AFM}$ range
init_{20}	3.8 ± 0.09	8.7 ± 0.13	4.9 ± 0.22	5.2			195	0.28	186	79	379	4 ± 2	32–95
a_{20}	3.0 ± 0.02	4.8 ± 0.05	1.8 ± 0.07	4.1	4.5	0.029 ± 0.003	275	0.17	268	197	434	4 ± 2	46–138
$i_{80}a_{20}$	3.7 ± 0.08	6.0 ± 0.07	2.3 ± 0.15	5.0			261	0.17	256	154	507	4 ± 2	45–133
$i^2_{80}a_{20}$	4.7 ± 0.24	7.4 ± 0.23	2.7 ± 0.47	6.4			203	0.22	197	98	367	4 ± 2	34–102
$i^3_{80}a_{20}$	6.0 ± 0.03	9 ± 0.37	3 ± 0.4	8.2			210	0.26	197	81	336	3 ± 2	40–200
i_{80}	5.0 ± 0.03	8.2 ± 0.16	3.2 ± 0.19	6.8	7.4	0.027 ± 0.008	184	0.20	181	115	279	4 ± 2	33–98
i^2_{80}	5.9 ± 0.06	9.1 ± 0.14	3.2 ± 0.2	8.0	7.2	0.02 ± 0.01	203	0.27	196	100	320	4 ± 2	30–91
i^3_{80}	7.0 ± 0.04	10 ± 1	3.4 ± 1.1	9.5			170	0.15	168	98	276	5 ± 2	24–57
i^4_{80}	8 ± 1	11 ± 2	3 ± 3	10.9			142	0.19	139	56	250	4 ± 2	23–69
init_{50}	3.4 ± 0.17	8.0 ± 0.33	4.6 ± 0.5	4.6	4.4	0.042 ± 0.006	234	0.26	224	115	405	4 ± 2	37–112
a^3_{50}	2.9 ± 0.03	4.5 ± 0.06	1.6 ± 0.09	4.0	4.0	0.037 ± 0.006	270	0.27	261	137	471	4 ± 2	38–113
a^4_{50}	2.5 ± 0.12	4.1 ± 0.19	1.6 ± 0.31	3.4	4.0	0.037 ± 0.004	287	0.27	277	153	478	5 ± 2	40–93
a^5_{50}	2.5 ± 0.10	4.0 ± 0.15	1.5 ± 0.25	3.4			297	0.21	285	163	560	6 ± 3	32–96
i^3_{50}	5.9 ± 0.2	15 ± 6	9 ± 6	8.0			181	0.24	178	106	325	4 ± 2	30–90
i^4_{50}	8 ± 0.6	12 ± 3	4 ± 4	11			170	0.19	168	110	295	4 ± 2	29–88

The main w_0 and w_1 values (columns 2–3) are obtained by fitting a linear function $\Phi = W − w_0/w_1 − w_0$ to the experimental phase separation data (Supplementary Figs. 6 and 7); error estimates are standard deviations derived from fitting (Quansoft ProFit, Levenberg–Marquardt algorithm). The biphasic regime size, $\Delta w = w_1 − w_0$, is given in column 4, and the comparison with w_1 predicted by Onsager theory (ignoring the variation with CNC content of the relation between CNC volume and mass concentration) is given in column 5. Column 6 shows $w_1(p_0)$, determined from the equilibrium pitch data by reading off W from the fitted curve at the highest experimental p_0, the fitting procedure yielding also the helical twisting power (HTP; error is standard deviation from fitting, same software and algorithm). The remaining columns hold data obtained from the AFM analysis of CNC sizes; $\bar{L}$ is the average length; $\bar{\imath}$ is the median length, ς is the length dispersity (definition in Supplementary Note 2) and $\bar{d}_{AFM}$ is the apparent lateral dimension. Because the uncertainty in d_{AFM} is so large, we give ranges rather than values for the aspect ratio $\bar{L}/\bar{d}_{AFM}$.
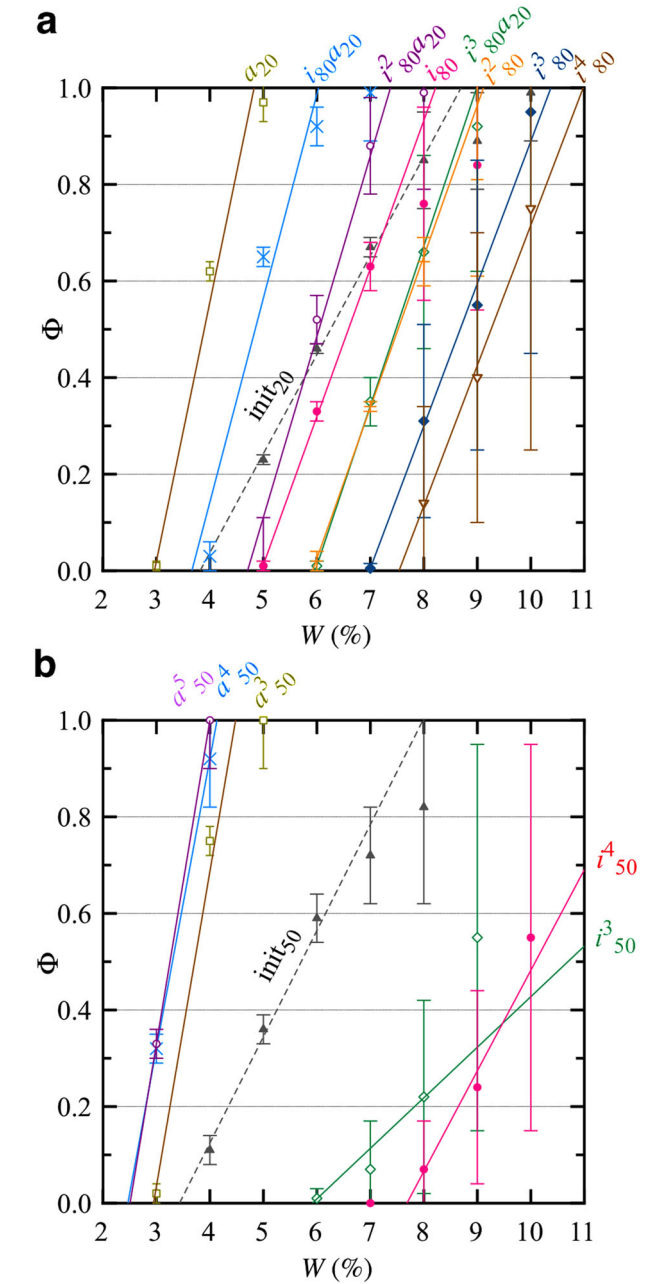

Fig. 2 The effect of fractionation on cholesteric–isotropic coexistence. Phase separation diagrams showing the volume fraction Φ of cholesteric (anisotropic) phase as a function of global sample CNC mass concentration W for each fraction of the 20/80 scheme (**a**) and the 50/50 scheme (**b**), respectively. Errors are dominated by the diverging time for phase separation as the CNC concentration approaches the threshold for kinetic arrest. Error bars are careful estimates of the resulting read-out errors, as detailed in Supplementary Note 4.

content, giving large errors in $\Phi(W)$ towards the higher end of the biphasic regime of pristine, unfractionated, suspensions and for the entire range of short-CNC fractions. This is the reason why the w_1 values (Table 1) and the phase separation curves (Fig. 2d) are so unreliable for the $i^3_{50}-$ and i^4_{50} fractions.

It is well established that a kinetically arrested state takes over beyond a limiting local CNC mass concentration w_k, terminating cholesteric self-assembly[1,21,28–30]. We recently demonstrated that w_k is unaffected by CNC fractionation[28]: it is determined by the ionic strength of the system, kinetic arrest setting in when the
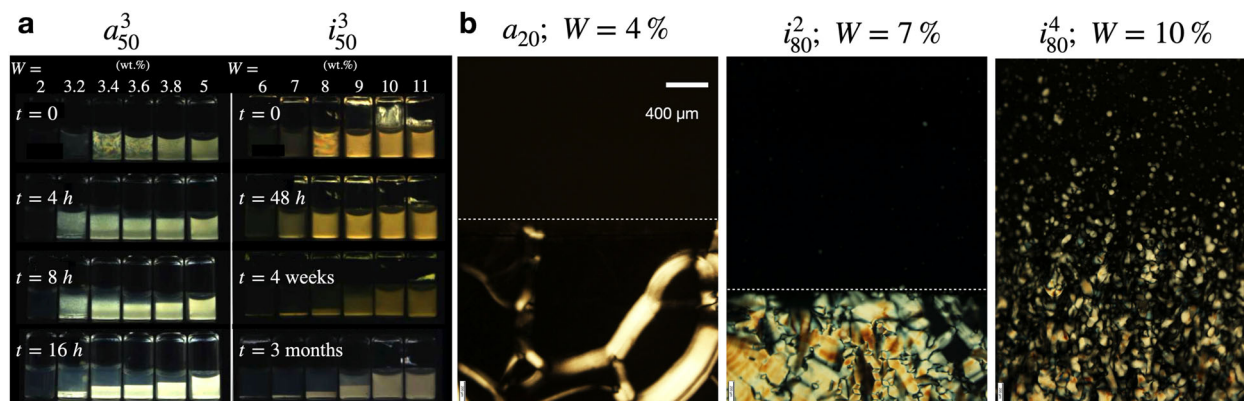
Fig. 3 Phase separation dynamics in suspensions with different CNC lengths. a Macroscopic phase separation (vial diameter: 11 mm) as a function of time t and global CNC concentration W for a_{50}^3 (long CNCs) and i_{50}^3 (short CNCs). While separation is near complete within a day for a_{50}^3, tactoids remain dispersed in the isotropic phase of i_{50}^3 even after several months. Time lapse movies of the processes are shown in Supplementary Movies 1 and 2. **b** The corresponding experiment on microscopic scale, with vertically stored (2 months) sealed flat capillaries filled with long (a_{20}), intermediate (i_{80}^2) and short (i_{80}^4) CNC fractions. Further details in Supplementary Note 5.

screening of the CNC surface charge by counter ions is so strong that colloidal stability is lost. For the CNC type studied here, $w_k \approx$ 12 wt.%. Earlier studies considered solely W when analysing the impact of kinetic arrest, ignoring the important fact that the local CNC content w is not the same in the isotropic and cholesteric phases of biphasic samples: $w \neq W$ everywhere. It is imperative for correct interpretation of data from biphasic suspensions to keep this difference in mind.

For our long-CNC fractions, we have $w_0 < w_1 \ll w_k$, ensuring that no kinetic arrest occurs in biphasic samples. We rapidly get macroscopic phase separation, yielding reliable data for long-CNC fractions in Fig. 2. We see this also at microscopic scale by investigating the polarising optical microscopy (POM) texture of vertically stored capillaries filled with representative fractions (Fig. 3b). The cholesteric texture at the bottom of the capillary filled with a_{20} shows a tactoid-free characteristic 'oily streak' texture (see Supplementary Note 5), distinguishing it from the isotropic phase at the top.

As $\bar{L}$ decreases in the other fractions, w_1 increases, approaching w_k which is not affected by changes in the CNC geometry. Because $w = w_1$ in the anisotropic phase, $w_1 \to w_k$ means that the viscosity within tactoids diverges, drastically slowing down the helical self-assembly dynamics[31]. For the intermediate i_{80}^2 fraction in Fig. 3b, we have $w_0@i_{80}^2 = 5.9$ wt.% $\ll w_k$ (Table 1), hence the isotropic phase stays at a reasonable viscosity, allowing tactoids to sink through it on the time scale of weeks. They form a sedimented cholesteric phase with the higher CNC concentration of $w_1@i_{80}^2 \approx 9.1$ wt.% (Table 1). This value, on the other hand, is so close to w_k that the high viscosity prevents the helix from adopting a uniform orientation within the time scale of the experiment. It retains an unoriented multi-domain character seeded by the many randomly arranged and viscous tactoids that formed it, see centre image in Fig. 3b.

With $\bar{L}$ decreased further in the i_{80}^4 fraction, the diverging separation time leaves an isotropic phase littered with tactoids even after several months (Fig. 3b, right). Those that reach the bottom hardly merge, yielding a heterogeneous texture. Because $w_1@i_{80}^4 \approx 11 \pm 2$ wt.% (Table 1), the tactoids are practically arrested internally. As for the coexisting isotropic phase, its CNC concentration is also high, $w_0@i_{80}^4 \approx 8 \pm 1$ wt.% (Table 1), rendering it so viscous that tactoid nucleation, growth and sedimentation do not complete in very long time, even 18 months being insufficient for the i_{50}^3 fraction, with slightly longer CNCs (Supplementary Fig. 9).

This inability of the two phases to separate macroscopically and of the cholesteric phase to adopt uniform order when w_1 increases is treacherous; samples in the biphasic regime, at global CNC concentration $W < w_1$, may appear fully liquid crystalline[32] and the equilibrium helix pitch, p_0, is difficult to establish accurately. Finally, it has significant consequences for the optics of films produced by drying CNC suspensions. The final two sections of this paper are devoted to these important issues relating quantitatively to the helical self-assembly in cholesteric suspensions.

Helical twisting power (HTP). With access to CNC fractions with reduced dispersity and different $\bar{L}$ we can investigate experimentally with unprecedented accuracy the dependence of the equilibrium helix pitch p_0 on the CNC content in the cholesteric phase (Fig. 4a, b) and even for the first time probe the effect of L on p_0 (Fig. 4c, d). A classic result from research on thermotropic liquid crystals[2] is that the inverse of the pitch, $1/p_0$, of a cholesteric phase created by adding a small concentration c of a chiral dopant to a non-chiral nematic host, is a linear function of c for small c. The proportionality constant is called the HTP, defined as $\text{HTP} = \lim_{c \to 0} 1/(p_0 c)$. In a colloidal cholesteric, the suspended chiral particles, in our case CNCs, simultaneously fill the dual roles of chiral dopant and mesogen. Moreover, since here we deal with electrostatically stabilised particles, any dependence on CNC content is simultaneously a dependence on ionic strength. Another important peculiarity is that the global CNC mass concentration W (or the corresponding average ionic strength) cannot generally replace c, since it is not representative of the cholesteric phase in biphasic samples. To the best of our knowledge, all previous reports on pitch versus CNC concentration (including our own) show data for highly disperse biphasic suspensions as a function of W; such data must be interpreted with care.

In Fig. 4a, we plot p_0 (measurement procedure described in Supplementary Note 6) versus the global CNC mass fraction W, but we do so for each fraction separately, including all long-CNC fractions and the two short-CNC fractions with the most reliable estimates of w_1: i_{80} and i_{80}^2. For all long-CNC suspensions, we find a constant pitch $p_0(w_1)$ for $w_0 < W < w_1$, reflecting the constant local cholesteric CNC mass concentration w_1 throughout the biphasic regime. Only for $W > w_1$ do we see a reduction in p_0, as the global and local cholesteric CNC mass concentrations then become identical. Moreover, we see in Fig. 4b that the data
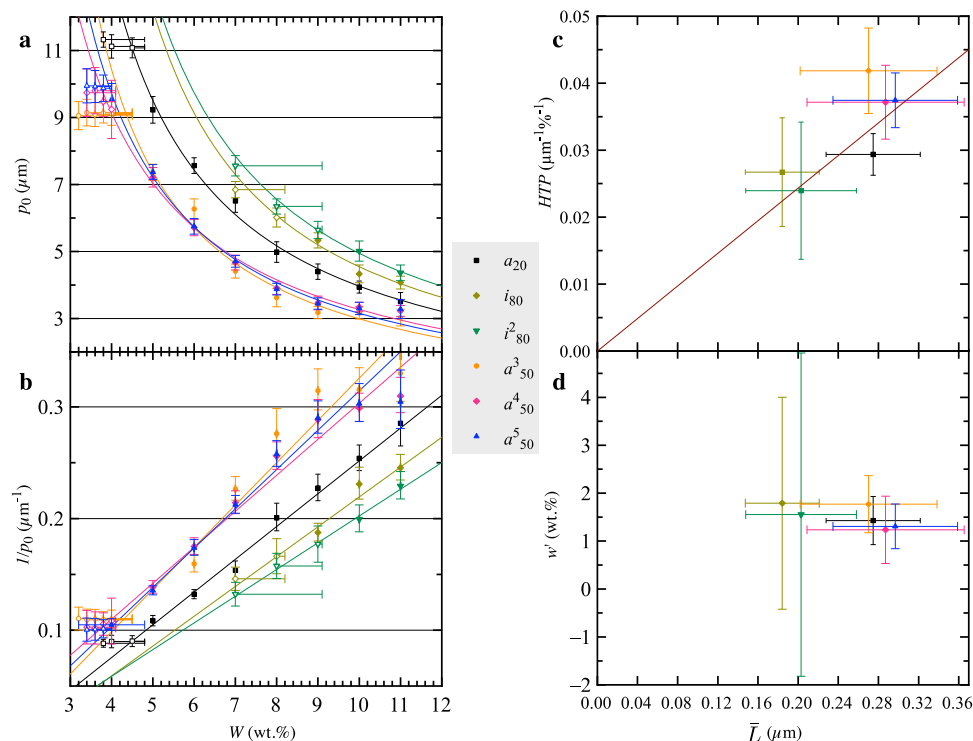
Fig. 4 Equilibrium helix pitch p_0 and its inverse as a function of global CNC concentration W for fractions with different average length $\bar{L}$, and the resulting functional fitting parameters. The lines in (**a**, **b**) are best fits of the function $1/p_0 = \mathrm{HTP}(W - w\prime)$ to experimental data, the fitting parameters plotted in (**c**, **d**) as function of $\bar{L}$. Data points at $W < w_1$ are plotted with empty symbols in (**a**, **b**), horizontal error bars representing the distance from w_1, whereas data points at $W \geq w_1$ are plotted with filled symbols. Vertical error bars for p_0 are standard deviations σ from $n = 40$–70 measurements in different sample areas, and for $1/p_0$ the error bars (asymmetric) represent $1/(p_0 \pm \sigma)$. In (**c**, **d**) the error bars are standard deviations from fitting, not considering possible systematic errors.

points for $W > w_1$ are well described by a linear relationship between $1/p_0$ and W up to a limiting value of $1/p_0 \approx 0.28\ \mu\mathrm{m}^{-1}$, corresponding to $p_0 \approx 3.6\ \mu\mathrm{m}$. This suggests that we can, indeed, define an HTP-value also for CNC suspensions.

For the short-CNC fractions, we find a p_0 that is significantly greater than that of long-CNC fractions at identical W, suggesting that HTP is greater for long than for short CNCs. Moreover, there is no initial plateau here, but p_0 continuously decreases from the lowest to the highest investigated W, with a quite good linear $1/p_0$ versus W dependence. We attribute the absence of plateau mainly to the lower reliability in the value for w_1, apparently overestimated even for i_{80} and $i^2{}_{80}$. This uncertainty is due to the greater dispersity of short-CNC fractions and to their slower dynamics, as discussed above.

Comparing with the classic model of thermotropic cholesterics, we obtain, for pitches greater than $p_0 \approx 3.6\ \mu\mathrm{m}$, excellent results of fitting (see Supplementary Note 7) a slightly modified linear relation to the experimental data:

$$1/p_0 = \mathrm{HTP}(W - w\prime);\ W > w_1,\ p_0 > 3.6\ \mu\mathrm{m}. \qquad (2)$$

We replace the chiral dopant concentration c with the CNC mass concentration W, reminding that Eq. (2) is valid only if $W > w_1$, and we introduce an offset CNC concentration $w\prime$, the interpretation of which we will come back to below. Because of the difficulty in establishing w_1 with certainty, especially for short-CNC fractions, we include also data points for $W < w_1$ in the fitting (w_1 values are in Table 1), but we then set $w_1 - W$ as the error range for the CNC mass concentration, as illustrated by horizontal error bars in Fig. 4a, b.

The fitting procedure confirms that HTP increases with increasing $\bar{L}$ (Fig. 4c), suggesting that the efficiency in transmitting chiral interactions along the helix scales with CNC length.

This contrasts with a theory for the colloidal cholesteric phase of finite-length double-stranded DNA 'rods', suggesting that a chiral torque (to which p_0 is inversely proportional) should decrease with rod length[33]. Our observation also appears to be opposite of the experimental findings of Beck-Candanedo et al.[34], who reported increasing p_0 with increasing CNC length at constant W. However, in that study the CNC length was varied by using different cellulose sources and varying the reaction conditions for extracting CNCs. While this produced different average lengths, one also expects variations in surface charge, degree of crystallinity, lateral dimensions and many other parameters, hence the changes in p_0 are not solely a result of varying CNC length. Moreover, no suspension had been fractionated, thus there was significant dispersity in length. Finally, as in prior reports of this kind, the authors did not consider the difference $w_1 > W$. The chosen $W = 7$ wt.% was in the biphasic regime for every fraction studied, in fact closer to the isotropic than the anisotropic phase. This means that the actual CNC content in the cholesteric phase, forming the helix that was being measured, varied significantly, a rough estimate based on the published phase separation diagrams being in the range from 10.5 to 13%.

Interestingly, Grelet and Fraden[35] found, in their study on cholesteric suspensions of rod-shaped mutant *fd*-viruses with different lengths, that the helix pitch decreased with increasing virus length, similar to our findings. While *fd*-virus is not CNC, there are many similarities, especially when considering the situation in colloidal suspension[1], and in this particular case the low dispersity of rod-shaped viruses might make them a better comparison to our study than many previous CNC works.

Concerning the form of the dependence of HTP on CNC length, the large uncertainty in the experimental values makes it difficult to make assertive statements. We note, however, that a
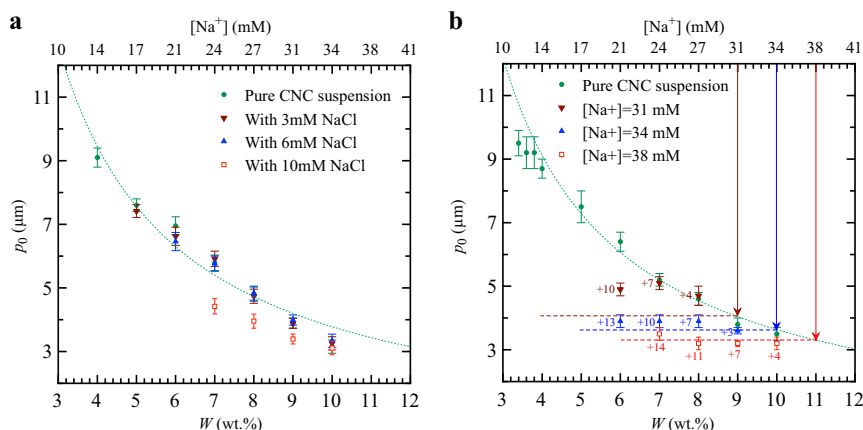
Fig. 5 Equilibrium helix pitch p_0 as a function of global CNC concentration W for suspensions enriched in long CNCs, without (green) and with varying concentrations of NaCl added. Panel (**a**) shows the result of adding the same amount of NaCl to all fractions, whereas panel (**b**) has different NaCl concentrations added to each sample (the amount in mM is indicated next to a data point) calculated such that a series has constant counter ion concentration, [Na$^+$]. The green line in each panel shows the best fit of Eq. (2) to the data without salt addition. Error bars are standard deviations σ from $n = 40$–70 measurements in different sample areas.

linear function extending from zero CNC length up to the studied values reproduces the experimental data quite well:

$$\mathrm{HTP} = k\bar{L}. \tag{3}$$

Fitting the function to the data using the standard deviations σ (HTP) and $\varsigma\bar{L}$, defined, tabulated and discussed in the Supplementary Note 2, we obtain a value of $k = 0.12$ for the only fitting parameter, the resulting linear curve plotted in Fig. 4c. This fit must be interpreted with care considering the large scattering in the data (see Supplementary Note 8).

Each CNC in suspension releases counter ions (here Na$^+$) to the aqueous continuous phase. In a first approximation, we consider the release per CNC constant, a simple calculation in Supplementary Note 9 yielding [Na$^+$] $\approx 0.343 W$ for our CNCs, the concentration given in mM. This means that any parameter depending on W might also depend on [Na$^+$]. The fact that the data series corresponding to different CNC lengths in Fig. 4a, b fall on different curves clearly shows that HTP is not primarily dependent on [Na$^+$], as no difference would have been seen between different CNC fractions in these diagrams should this have been the case. However, the helix pitch p_0 could depend on [Na$^+$].

In a first attempt to distinguish the impact of W and [Na$^+$] on p_0, we show pitch data for two further suspensions enriched in long CNCs, following three generations of 50–50 fractionation from a different experiment, in the pristine state as well as with varying concentrations of NaCl dissolved in the water, see Fig. 5. In panel (a), we compare p_0 for the pristine suspension with p_0 when 3, 6 or 10 mM NaCl is added to every vial, respectively. We find that the two lowest salt concentrations have negligible impact, while 10 mM shortens the helix somewhat. In panel (b), we have instead added varying amounts of NaCl to each sample, calculated in such a way that we get one series each with [Na$^+$] = 31, 34 and 38 mM, respectively, corresponding to the counter ion content of CNC suspensions without added NaCl at $W = 9$, 10 and 11 wt.%. We see that [Na$^+$] = 31 mM (brown down triangles) reduces the pitch at $W = 6$ wt.%, but not at 7–8 wt.%, where p_0 is identical to the values without added salt, and in no case is p_0 as low as in the pure CNC suspension at [Na$^+$] = 31 mM (highlighted with a brown dashed horizontal line in Fig. 5b). However, for [Na$^+$] = 34 mM (blue up triangles) the pitch becomes nearly independent of W and at $W = 9$ wt.%, p_0 is at the value corresponding to the pure CNC suspension at

[Na$^+$] = 34 mM (highlighted with a blue dashed horizontal line). Finally, with [Na$^+$] = 38 mM (red squares) p_0 is at or even below the pitch of the pure CNC suspension at [Na$^+$] = 38 mM (highlighted with a red dashed horizontal line) for $W \geq 8$ wt.%, and for 7 wt.% it is only slightly longer.

While the results clearly show that dissolved ions can have major impact on p_0, the varying behaviour suggests a complex relationship; low salt additions have negligible impact, but at salt content approaching that of kinetic arrest ($w_k \approx 12$ wt.% is equivalent to [Na$^+$] = 41 mM) the counter ions seem to dominate the behaviour. As we have previously shown[28] that CNC aggregation starts at salt concentrations well below the limit for kinetic arrest, the changing behaviour may be related to a change in the effective 'rod' characteristics at high salt content. In future, more detailed investigations are needed to fully elucidate the impact of the counter ions.

At the scale of individual CNCs, the primary result of an increase in counter ion concentration is to reduce the Debye screening length κ^{-1}, which adds to the physical CNC size to define the effective 'rod' in a CNC suspension. To make the following discussion tractable, we now approximate the CNC shape as cylindrical, representing it with an average diameter d. Because $L \gg \kappa^{-1}$ the impact on the length is negligible, but the impact on the diameter is significant. As we raise [Na$^+$], we thus reduce the effective volume fraction ϕ at a certain value of W, but at the same time we reduce ϕ_0 and ϕ_1 since the aspect ratio increases when d decreases at constant L. Both phenomena affect the experimental stability limits w_0 and w_1 of the isotropic and chiral nematic phase, respectively, in antagonistic ways, hence the overall impact is non-trivial. We model the impact quantitatively in Supplementary Note 9, with particular emphasis on the effect of [Na$^+$] on w_1, since pitch data can only be reliably compared if $W > w_1$. For a long-rod suspension with $w_1 = 3.9$ wt.% prior to salt addition, we find that the threshold increases to $w_1 = 4.2$, 4.4 and 4.7 wt.%, respectively, for 3, 6 and 10 mM added NaCl, respectively (Supplementary Fig. 18). For the series with constant [Na$^+$] we find $w_1 = 4.9$, 5.0 and 5.1 wt.%, respectively, for [Na$^+$] = 31, 34 and 38 mM, respectively (Supplementary Fig. 19). We can thus safely conclude that all data in Fig. 5 correspond to fully liquid crystalline samples, hence the comparisons between different series are valid.

We can now return to the question of the physical relevance of the fitting parameter $w' \approx 1.5$ wt.%, fairly independent of CNC

fraction. A first possible interpretation is that w' may correspond to a maximum average separation between CNCs for chiral interactions to be transmitted through the isotropic solvent, in our case water. The helix could thus start developing only once $W > w'$. Perhaps more likely is that w' may correspond to a value of $[Na^+]$ that is so low that the electrostatic repulsion, over a range κ^{-1}, effectively screens off chiral interactions between CNCs. This interpretation would resonate well with the model of Araki and Kuga[36] in their study of the effect of electrolyte addition to cholesteric CNC suspensions.

The offset represented by w' is interesting in its potential ability to explain why some colloidal suspensions of chiral nanorods, a famous example being tobacco mosaic virus, show nematic order but no trace of helix formation: if $W < w'$ the helix does not develop. We find support for this interpretation in the study of bacterial CNC with extreme aspect ratio by Araki and Kuga[36], with an exceptionally low value of $w_0 \approx 0.1$ wt.%. Since no fractionation was employed in that study there is no experimental value for w_1, but based on Onsager's theory we can conclude that $w_1 \ll w' \approx 1.5$ wt.%. Indeed, Araki and Kuga found that suspensions prepared at $W = 1.2$ wt.% showed nematic order but no helix development. However, if they added NaCl to the suspension and raised the CNC mass concentration to 1.6 wt.%, the textures revealed that a helix developed. The salt-free suspension may have had a CNC mass concentration in the anisotropic phase lower than w', but with salt addition it rose above w' (because salt addition raises w_1), thus allowing the helix to develop.

Summarising these results, we propose a quantitative relation between helix pitch, average rod length and chiral rod mass concentration in colloidal cholesterics that should be approximately valid at least for CNC suspensions in water:

$$1/p_0(\bar{L}, W) = k\bar{L}(W - w') \approx 0.12\bar{L}(W - 1.5); W > w_1, p_0 > 3.6 \, \mu m. \tag{4}$$

In doing so, we strongly caution that this is a purely empirical derivation, based on multiple generations of fitting, starting from experimental data with limitations, hence it should be considered primarily a stimulus for discussion and further research at this stage. Future work with more fractions, with narrower CNC length distributions and with carefully designed studies with controlled salt addition will be necessary to corroborate this suggestion, hopefully also supported by theoretical treatments.

We end this section by briefly discussing the observed validity limit of Eqs. (2) and (4) at $p_0 \approx 3.6 \, \mu m$. This is not an artefact arising from measurements being done prematurely, before the helix reaches equilibrium, because fitting works well up to and including $W = 11$ wt.% for fractions a_{20}, i_{80} and i_{80}^2, for which $p_0 > 3.6 \, \mu m$ in the investigated range. In contrast, fitting fails for $W \geq 10$ wt.% for a_{50}^3, a_{50}^4 and a_{50}^5, where $p_0(W = 9 \text{ wt\%}) \approx 3.6 \, \mu m$. For higher W the pitch decays approximately exponentially towards a lower saturation value p_0^{min}. A simple function on the form:

$$p_0 = Ae^{-W} + p_0^{min} \tag{5}$$

yields a good fit to the $W = 9$–11% range of the a_{50}^5 data with $A = 1.68 \times 10^3 \, \mu m$ and $p_0^{min} \approx 3.24 \, \mu m$. The observation of a lower saturation value for p_0 matches well the observations of Bruckner et al.[31] for CNC suspensions in non-aqueous solvents. In that study, a minimum pitch of $p_0^{min} \approx 3 \, \mu m$ was found for CNCs suspended in N-methylformamide. To rationalise why a lower saturation value may exist, we consider what happens at the nanoscopic scale in a cholesteric suspension. The twisting between adjacent CNCs is quite small[37], on the order of 1°. The competition to the chiral interactions, which promote twist,

from van der Waals and direct inter-CNC hydrogen bonding interactions, both promoting parallel alignment, should thus not be very strong. We propose that the lower saturation of p_0 may correspond to a twist angle between adjacent CNCs that is too high for this approximation to hold. The effect may be additionally strengthened by the reduced impact of electrostatic repulsion (promoting twisting as an orthogonal arrangement between adjacent CNCs would minimise electrostatic energy) at high ionic strength. A continued pitch decrease following Eqs. (2) and (4) would not be possible, instead yielding an exponential decrease towards a saturation value. Future theoretical efforts are needed to fully investigate this issue.

Dried films. Using Eqs. (4) and (5), we can estimate p_0 for situations where experimental data are challenging to obtain, in particular at $W = w_k \approx 12\%$, where a suspension gets kinetically arrested. We compare this with experimental data on p in dried films obtained by evaporating the water from different CNC suspensions. Following Frka-Petesic et al.[29], a vertically oriented helix (vertical **m**) is compressed by a maximum factor $100/\phi'_k$ upon evaporation, where ϕ'_k is the volume concentration of cellulose at kinetic arrest. In Supplementary Note 10, we establish $\phi'_k \approx 8.3$ vol.% for $w_k = 12$ wt.%, hence we expect a $100/8.3 = 12$-fold compression for vertical **m**.

We dry films from the extreme fractions of the 50/50 scheme, the a_{50}^5 long-CNC (L) and the i_{50}^4 short-CNC (S) suspension. With $\bar{L}^S \approx 0.17 \, \mu m$ for i_{50}^4 (Table 1), Eq. (4) yields an expected equilibrium pitch $p_0^S(w_k) \approx 4.7 \, \mu m$ at kinetic arrest. For a_{50}^5, Eq. (4) predicts p_0 below the validity range, hence we use Eq. (5) to obtain $p_0^L(w_k) \approx 3.2 \, \mu m$. Considering the compression during drying beyond kinetic arrest, these numbers yield $p_f^L = 0.27 \, \mu m$ and $p_f^S = 0.39 \, \mu m$ for the final (f) pitch in films formed from a_{50}^5 and i_{50}^4, respectively. With $\bar{n} \approx 1.6$ for CNC[38] and normal incidence illumination ($\theta = 0°$), Bragg's law, Eq. (1), thus predicts reflection at air wavelengths $\lambda^L \approx 0.43 \, \mu m$ (violet) and $\lambda^S \approx 0.62 \, \mu m$ (orange) for long- and short-CNC films, respectively.

As reported by Zhao et al.[39] and Tran et al.[40], it is imperative to slow down water evaporation to obtain films with good optical quality. We follow the Zhao et al. method, covering the CNC suspension droplet by a thin layer of hexadecane, starting with $W = 3$ and 6 wt.%, respectively. Representative excerpts of optical and electron microscopy images of the 3 wt.% films are shown in Fig. 6, complemented by Supplementary Notes 11 and 12. Films dried from a_{50}^5 reflect dark violet for $W = 3$ and 6 wt.%, in perfect agreement with expectation. There is no mosaic texture, indicating that tactoids were fully merged at kinetic arrest, and the reflection is perfectly left-handed circularly polarised, in line with a vertically aligned arrested CNC helix[29]. In contrast, films formed by short CNCs in i_{50}^4 appear predominantly red at $W = 3$ wt.%, the reflection shifting radially from green to infrared in the film dried from $W = 6$ wt.%. Both i_{50}^4 films have a mosaic character, indicating unmerged tactoids at kinetic arrest, and imperfect circular polarisation.

We fracture films made from $W = 3$ wt.% suspensions of a_{50}^5 and i_{50}^4 and image the surface by scanning electron microscopy (SEM; Fig. 6d, h and Supplementary Figs. 22 and 23). The former film, from long CNCs, shows a near-perfect uniform vertical helix orientation **m** with a low value for the final helix pitch, $p_f^L \approx 0.25 \pm 0.02 \, \mu m$ throughout the film, thus an excellent match to our prediction. In contrast, the i_{50}^4 film (short CNCs) has well-defined helical order only near the boundaries, with an average $p_f^S \approx 0.48 \pm 0.04 \, \mu m$, significantly higher than prediction. Surprisingly, the orientation of the helix—where it has developed—is

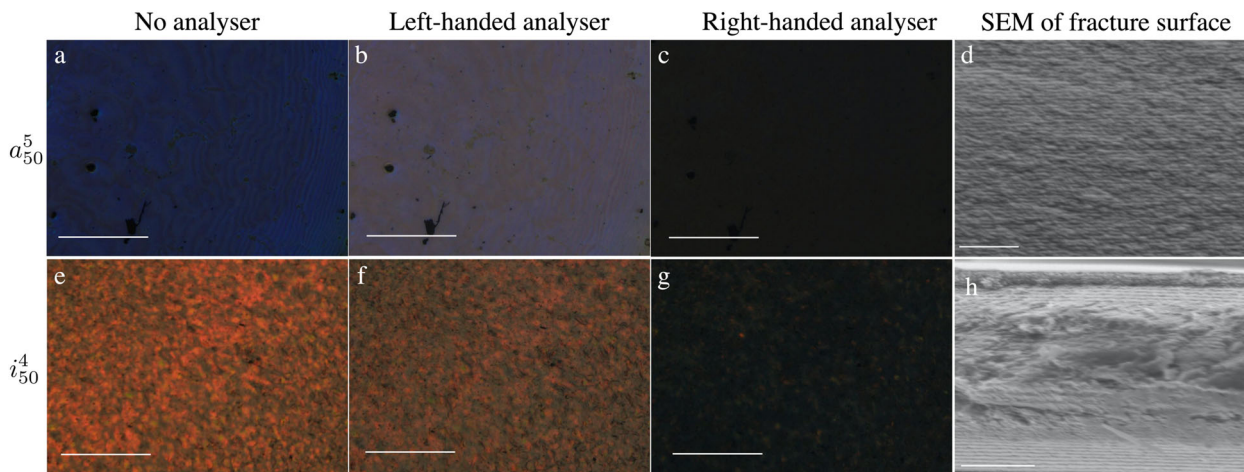| No analyser	Left-handed analyser	Right-handed analyser	SEM of fracture surface

Fig. 6 Optical and electron microscopy characterization of films obtained by drying suspensions of long and short CNCs, respectively. Films dried from $W = 3$ wt.% suspensions of long (top) and short (bottom) CNCs as imaged by POM (**a–c**, **e–g**, scale bar 500 µm) and SEM (**d**, scale bar 2 µm; **h**, scale bar 5 µm). The long-CNC suspension produces uniform vertical helix orientation **m** and a final pitch as predicted from equilibrium data. The film from short CNCs has non-uniform texture and cross section, with final pitch much longer than predicted.

vertical also in the i^4_{50} film. The helix has apparently been aligned by the bottom substrate and top oil interface, both promoting planar alignment of **n** and thus vertical **m**[1]. The imperfect circular polarised reflection should thus have a different origin than the distortion due to inclined **m** in tactoids discussed by Frka-Petesic et al.[29]. We conjecture that the birefringence from the non-helical bulk of the film (Fig. 6h) may change the polarisation of the right-handed circularly polarised light transmitted by the top helical regime, such that it is partially reflected at the bottom.

As **m** is not inclined, it has been subjected to full vertical compression during the final water evaporation, hence the pitch at kinetic arrest should have been $p^S_k = 12 \cdot 0.48 \approx 6$ µm. Clearly, the drying process, even under hexadecane, has been much too fast for the slow dynamics of the short-CNC cholesteric phase, preventing it to even get close to the equilibrium pitch at kinetic arrest, $p^S_0(w_k)$. The actual pitch at kinetic arrest, $p^S_k \approx 6$ µm, would according to Eq. (4) correspond to $p^S_0(\bar{L}^S \approx 0.17$ µm, $W \approx 9.7$ wt.%). This CNC content may be considered an effective w_1 for the i^4_{50} fraction. In Supplementary Note 9 (Supplementary Fig. 17), we are able to reproduce this value analytically for $\bar{L}^S \approx 0.17$ µm, using the very reasonable approximation $d^S = 5$ nm for dry CNCs. The offset from Table 1 illustrates how unreliable an estimate of w_1 is when it approaches w_k and when the dispersity is not negligible. We thus conclude that the cholesteric phase forms with $p^S_0(w_1 \approx 9.7$ wt.%) and its viscosity is then already so high that the speed of water removal allows no further pitch reduction towards lower p_0 as the CNC mass concentration increases, until the onset of kinetic arrest.

Note that the initial $W = 3$ wt.% $\ll w_0@i^4_{50} = 8$ wt.%, hence the droplet from which the film is formed starts out fully isotropic. As cholesteric phase nucleates, it is likely to do so (with vertical **m**) at the bottom substrate and the top oil interface, where the symmetry breaking has an ordering influence. The cholesteric phase thus grows inwards from the top and bottom as water escapes from the droplet. However, since cholesteric phase nucleation cannot start before $W = w_0@i^4_{50}$, the viscosity of the isotropic phase is so high that this development of cholesteric order is slow. Hence, much of the interior has not had the chance to order prior to kinetic arrest, explaining the largely non-uniform bulk.

In summary, we have presented an efficient and scalable method for fractionating CNC suspensions according to length L, yielding data suggesting that the HTP grows linearly with CNC length. Fractions with low $\bar{L}$ have very slow dynamics, requiring months to complete the isotropic–cholesteric separation and to reach equilibrium helix pitch. Failure to acknowledge this kinetic impact, and the fact that the cholesteric CNC mass concentration w_1 is greater in biphasic samples than the global mass concentration W, causes misunderstandings regarding phase diagram and helix pitch behaviour. We anticipate that access to series of fractionated CNC suspensions with stepwise increasing $\bar{L}$ and low dispersity, together with accurate values of w_0 and w_1 for each fraction, will allow the production of uniform films with colour continuously tuneable from the UV, throughout the visible spectrum, into the IR. The time of drying, set by the relative humidity (RH) or the amount of oil covering a droplet, should be adjusted to $\bar{L}$ in each droplet. This will speed up the production of violet–blue films from long-CNC suspensions, while giving enough time for achieving acceptable optical quality of orange–red films made from short-CNC suspensions. We are currently refining our fractionation, characterisation and film-drying methods to this end.

Methods

Preparation of initial CNC suspension. The starting CNC suspensions with Na^+ counter ions (CAS number 9004-34-6) were purchased from USDA Forest lab, University of Maine (USA), properly stored under refrigeration until use. The batch used for the 50/50 fractionation was the same as in our previous fractionation study[28]; see the Supplementary Information of that paper for a complete characterisation of the batch. A different batch was used for the 20/80 fractionation scheme and its characterisation is provided in Supplementary Note 1 of this paper. The two batches are highly comparable, the concentration of sulphate half-ester groups determined by conductometric titration corresponding to 1 wt.%. More details of the preparation procedure and product specification provided by the supplier can be found at https://umaine.edu/pdc/nanocellulose/nanocellulose-basics/.

The as-received sample at $W = 11$ wt.% was diluted to 6 wt.% by the addition of ultra-pure water and sonicated for 70 s using an ultrasonic probe (7 mm diameter titanium tip, Dr. Hielscher UP200St; the sonication power was identical to that calculated in ref. [28]). Each initial CNC series ($init_{20}$ and $init_{50}$) was then prepared with mass concentrations $W = 1$–11 wt.% in integer steps, $W > 6$ wt.% achieved by evaporation and $W < 6$ wt.% by dilution with ultra-pure water.

Fractionation. In the 20/80 fractionation procedure (Fig. 1a), 800 g of the disperse pristine CNC suspension, prepared as described above, at a global mass concentration $W = 5.5$ wt.% (see Supplementary Note 3 for an account of how the target concentrations are established), is filled into a separatory funnel, which is closed. The suspension is left standing, resulting in clear separation (Fig. 1d, e) of ~20 vol.% anisotropic (cholesteric) phase and ~80 vol.% isotropic phase after ~7 days. After another 7 days, the anisotropic phase is decanted into a vial by opening the stop cock, thereby creating the a_{20} fraction. A sample of the isotropic

supernatant, i_{80}, is retained for further investigation, while the rest is transferred to a beaker, where it is concentrated under stirring until $W = 6$ wt.%. The suspension is then transferred back to the separatory funnel where it is left undisturbed. For this new suspension, which lacks the longest CNCs of the pristine suspension, the slightly increased W (6% instead of 5.5%) again leads to separation into 20% anisotropic and 80% isotropic phase. After a total of 14 days in the closed funnel, the macroscopic phase separation is again completed, the denser anisotropic phase sedimented at the bottom. We extract also this phase, giving us the $i_{80}a_{20}$ fraction. The remainder we refer to as i_{80}^2. We repeat this procedure another two times, giving us additionally $i_{80}^2a_{20}-$ and $i_{80}^3a_{20}$ from each anisotropic phase separation (after 14 days in the separatory funnel) as well as i_{80}^3- and i_{80}^4 from the respective remaining isotropic phase.

For the 50/50 scheme (Fig. 1b), 800 g of the disperse pristine CNC suspension at a global mass concentration $W = 6$ wt.% CNC is filled into a separatory funnel, with the target of a volume fraction of 50% between isotropic and anisotropic phases. The funnel is closed and after 14 days the lower half is extracted (a_{50}), somewhat enriched in long CNCs. We then dilute this fraction to $W = 5.5$ wt.% by adding ultra-pure water, again with a target of 50% anisotropic phase separating, after which we place it in the separatory funnel. After closing the funnel, the suspension is left there for 14 days. At the same time the isotropic fraction obtained in the first step (i_{50}) is concentrated to $W = 7$ wt.% in a beaker under room conditions, with the aim to obtain 50/50 anisotropic/isotropic separation in this fraction, somewhat enriched in short CNCs. The procedure is repeated four times, each extraction done at a CNC concentration yielding 50% by volume of each phase (details in Supplementary Note 3). When referring to data produced using this method, the anisotropic fractions are described as a_{50}^n and the isotropic fractions as i_{50}^n, where n is the number of consecutive extractions. The waiting times prior to extraction of the separated anisotropic phase were 14 days, for $n = 2$–5.

Establishing of the phase separation diagram. Series of global CNC mass concentrations W are prepared by first concentrating each CNC fraction using mild mechanical stirring at room temperature. Once the CNC concentration is high enough ($W \approx 12$ wt.%), each fraction is distributed into different vials, diluted in different proportions with ultra-pure water to achieve the different targeted concentrations (normally $W = 1$–12 wt.% in integer steps). The vials are left standing undisturbed for several weeks, and once phase separation is deemed complete, the volume fraction Φ of cholesteric phase is determined for each W of each fraction by measuring the height of the cholesteric phase compared to the height of the entire sample from images of the vials captured between crossed polarisers (Supplementary Note 4).

We fit (Quansoft ProFit, Levenberg-Marquardt algorithm) a linear function $\Phi = W - w_0/w_1 - w_0$, based on classic Onsager theory, to the experimental data. This ignores the changing effect of ionic screening[1], becoming increasingly significant for increasing W. We consider this approximation acceptable because of the reduced dispersity in each fraction, although it means that the w_1 value from the fit corresponding to the longest CNCs in the fraction, which define the experimentally observed w_0 value, is always somewhat underestimated.

Determination of the equilibrium chiral nematic pitch p_0 of CNC samples. CNC suspensions were filled into 5 cm long capillaries with a rectangular cross section of 0.20×4 mm^2 (CM Scientific Ltd.). Both capillary extremes were sealed with Super Mix Metal epoxy glue and stored vertically for minimum 1 month before imaging. The anisotropic fractions were imaged between crossed polarisers in transmission mode on an Olympus BX51 microscope equipped with an Olympus DP73 camera. The pitch was determined from regions with well-developed fingerprint texture (horizontal helix) as $p_0 = 2l/m$, where l is the distance along the helix considered and m is the number of fingerprint lines traversed along l. A minimum of 40, more often about 70, measurements were done on each capillary, in different locations, to get sufficient statistics. To establish HTP and w', we fit a $1/p_0 = \mathrm{HTP}(W - w')$ function to the experimental p_0 data (Quansoft ProFit, Levenberg-Marquardt algorithm).

Atomic force microscopy (AFM). A Multi-mode V AFM was used in tapping mode to image the different fractionated CNC samples with probes from Budget Sensors (Tap300 Al-G, force constant 40 Nm^{-1} and resonance frequency 300 kHz). For the preparation of the sample, a 20 μL volume of cationic poly-L-lysine solution (0.01 vol.%) was placed on the surface of a freshly cleaved negatively charged mica (NanoAndMore GmbH). Afterwards, the mica surface was rinsed with ultra-pure water and dried with compressed air. A volume of 20 μL of CNC suspension at 0.002 wt.% was deposited onto the treated cleaved mica surface. After 3 min, the mica was rinsed with ultra-pure water and dried with air. Finally, the dried sample was placed into a vacuum oven overnight at 40 °C before imaging. The statistical analysis is done by measuring the lengths and apparent lateral dimensions of 200 CNCs from each fraction from the AFM data and fitting (Quansoft ProFit, Levenberg-Marquardt algorithm) a log-normal function to the distributions (measurement routine and fitting are described in detail in the Supplementary Note 2).

Preparation of CNC solid films. 20 μL drops of CNC suspensions were deposited on untreated rectangular glass coverslips (20×20 mm, Carl Roth) using a micropipette. In order to avoid water evaporation during the deposition, all experiments were carried out inside a glove box, which was maintained at 22 °C and 90% RH. Afterwards, the CNC drops were completely covered with hexadecane and removed from the glove box to continue the drying process at ambient conditions (22 °C and 40% RH) for 3 weeks.

Characterisation of CNC films. *Scanning electron microscopy (SEM)*: For imaging the cross section of the dried CNC films, each sample was fractured by scribing a line on the back part of the glass coverslip and cracking the sample. Half of the film was attached to a solid support using carbon tape, with the fracture oriented in the direction of imaging. The fractured film was then coated with a 9 nm gold layer. All the cross sections were imaged with a JEOL (JSM-6010) electron microscope at operating voltage of 10 kV, 10 cm working distance and 130 °C filament temperature.

Polarising optical microscopy (POM): An Olympus BX51 polarising microscope in reflection mode was used for the investigation of the optical properties of the films. For the detection of circular polarisation, a quarter wavelength retardation plate was inserted between the crossed polarisers. The polariser and analyser were both rotated ±90° for switching between right- or left-handed circular polarisation illumination and analysis. The illumination always had the same handedness as the analysis.

Data availability
The raw data that support the findings of this study, beyond what is included in the main article and in the Supplementary Information, can be downloaded from a repository at https://osf.io/3rhn5/?view_only=75424b17fc744d9c9a5dc7618c846226. These files relate to Table 1, Figs. 1c, f, 2, 4 and 5, Supplementary Figs. 5–7 and 10–15 and Supplementary Table 2.

References
1. Schütz, C. et al. From equilibrium liquid crystal formation and kinetic arrest to photonic bandgap films using suspensions of cellulose nanocrystals. *Crystals* **10**, 199 (2020).
2. Kitzerow, H. & Bahr, C. *Chirality in Liquid Crystals (Partially Ordered Systems)* (Springer, 2000).
3. Srinivasarao, M. Nano-optics in the biological world: beetles, butterflies, birds, and moths. *Chem. Rev.* **99**, 1935–1961 (1999).
4. Mitov, M. Cholesteric liquid crystals in living matter. *Soft Matter* **13**, 4176–4209 (2017).
5. Frka-Petesic, B. & Vignolini, S. So much more than paper. *Nature Photon.* **13**, 365–367 (2019).
6. Vignolini, S. et al. Pointillist structural color in Pollia fruit. *Proc. Natl Acad. Sci.* **109**, 15712–15715 (2012).
7. Ling, S., Kaplan, D. L. & Buehler, M. J. Nanofibrils in nature and materials engineering. *Nat. Rev. Mat.* **3**, 18016 (2018).
8. Ilca, S. L. et al. Multiple liquid crystalline geometries of highly compacted nucleic acid in a dsRNA virus. *Nature* **570**, 252–256 (2019).
9. Leforestier, A. & Livolant, F. The bacteriophage genome undergoes a succession of intracapsid phase transitions upon DNA ejection. *J. Mol. Biol.* **396**, 384–395 (2010).
10. Minsky, A., Shimoni, E. & Frenkiel-Krispin, D. Stress, order and survival. *Nat. Rev. Mol. Cell Biol.* **3**, 50–60 (2002).
11. Tidu, A. et al. Highly concentrated collagen solutions leading to transparent scaffolds of controlled three-dimensional organizations for corneal epithelial cell colonization. *Biomater. Sci.* **6**, 1492–1502 (2018).
12. Bouligand, Y. Liquid crystals and biological morphogenesis: ancient and new questions. *C. R. Chim.* **11**, 281–296 (2008).
13. Nyström, G., Arcari, M. & Mezzenga, R. Confinement-induced liquid crystalline transitions in amyloid fibril cholesteric tactoids. *Nat. Nanotechnol.* **13**, 330–336 (2018).
14. Agez, G., Bayon, C. & Mitov, M. Multiwavelength micromirrors in the cuticle of scarab beetle Chrysina gloriosa. *Acta Biomater.* **48**, 357–367 (2017).
15. Weaver, J. C. et al. The stomatopod dactyl club: a formidable damage-tolerant biological hammer. *Science* **336**, 1275–1280 (2012).
16. Almeida, A. P. C. et al. Cellulose-based biomimetics and their applications. *Adv. Mater.* **30**, e1703655 (2018).
17. Klemm, D. et al. Nanocelluloses: a new family of nature-based materials. *Angew Chem.* **50**, 5438–5466 (2011).

18. Revol, J. -F., Godbout, L. & Gray, D. G. Solid self-assembled films of cellulose with chiral nematic order and optically variable properties. *J. Pulp Pap. Sci.* **24**, 146–149 (1998).

19. Wang, P. X., Hamad, W. Y. & MacLachlan, M. J. Structure and transformation of tactoids in cellulose nanocrystal suspensions. *Nat. Commun.* **7**, 11515 (2016).

20. Park, J. H. et al. Macroscopic control of helix orientation in films dried from cholesteric liquid-crystalline cellulose nanocrystal suspensions. *ChemPhysChem* **15**, 1477–1484 (2014).

21. Lagerwall, J. P. F. et al. Cellulose nanocrystal-based materials: from liquid crystal self-assembly and glass formation to multifunctional thin films. *NPG Asia Mater.* **6**, e80 (2014).

22. Tatsumi, M., Teramoto, Y. & Nishio, Y. Polymer composites reinforced by locking-in a liquid-crystalline assembly of cellulose nanocrystallites. *Biomacromolecules* **13**, 1584–1591 (2012).

23. Shopsowitz, K. E., Qi, H., Hamad, W. Y. & MacLachlan, M. J. Free-standing mesoporous silica films with tunable chiral nematic structures. *Nature* **468**, 422–425 (2010).

24. Saha, P. & Davis, V. A. Photonic properties and applications of cellulose nanocrystal films with planar anchoring. *ACS Appl. Nano Mater.* **1**, 2175–2183 (2018).

25. Onsager, L. The effects of shape on the interaction of colloidal particles. *Ann. N. Y. Acad. Sci* **51**, 627–659 (1949).

26. Zhang, S. J., Kinloch, I. A. & Windle, A. H. Mesogenicity drives fractionation in lyotropic aqueous suspensions of multiwall carbon nanotubes. *Nano Lett.* **6**, 568–572 (2006).

27. Dong, X. M., Revol, J. F. & Gray, D. G. Effect of microcrystallite preparation conditions on the formation of colloid crystals of cellulose. *Cellulose* **5**, 19–32 (1998).

28. Honorato-Rios, C. et al. Fractionation of cellulose nanocrystals: enhancing liquid crystal ordering without promoting gelation. *NPG Asia Mater.* **10**, 455–465 (2018).

29. Frka-Petesic, B., Kamita, G., Guidetti, G. & Vignolini, S. Angular optical response of cellulose nanocrystal films explained by the distortion of the arrested suspension upon drying. *Phys. Rev. Mater.* **3**, 045601 (2019).

30. Honorato-Rios, C. et al. Equilibrium liquid crystal phase diagrams and detection of kinetic arrest in cellulose nanocrystal suspensions. *Front. Mater.* **3**, 21 (2016).

31. Bruckner, J. R., Kuhnhold, A., Honorato-Rios, C., Schilling, T. & Lagerwall, J. P. Enhancing self-assembly in cellulose nanocrystal suspensions using high-permittivity solvents. *Langmuir* **32**, 9854–9862 (2016).

32. Hirai, A., Inui, O., Horii, F. & Tsuji, M. Phase separation behavior in aqueous suspensions of bacterial cellulose nanocrystals prepared by sulfuric acid treatment. *Langmuir* **25**, 497–502 (2009).

33. Kornyshev, A. A., Leikin, S. & Malinin, S. V. Chiral electrostatic interaction and cholesteric liquid crystals of DNA. *Eur. Phys. J. E* **7**, 83–93 (2002).

34. Beck-Candanedo, S., Roman, M. & Gray, D. Effect of reaction conditions on the properties and behavior of wood cellulose nanocrystal suspensions. *Biomacromolecules* **6**, 1048–1054 (2005).

35. Grelet, E. & Fraden, S. What is the origin of chirality in the cholesteric phase of virus suspensions. *Phys. Rev. Lett.* **90**, 198302 (2003).

36. Araki, J. & Kuga, S. Effect of trace electrolyte on liquid crystal type of cellulose microcrystals. *Langmuir* **17**, 4493–4496 (2001).

37. Schütz, C. et al. Rod packing in chiral nematic cellulose nanocrystal dispersions studied by small-angle X-ray scattering and laser diffraction. *Langmuir* **31**, 6507–6513 (2015).

38. Parker, R. M. et al. The self-assembly of cellulose nanocrystals: hierarchical design of visual appearance. *Adv. Mater.* **30**, 1704477 (2017).

39. Zhao, T. H. et al. Printing of responsive photonic cellulose nanocrystal microfilm arrays. *Adv. Funct. Mater.* **29**, 1804531 (2018).

40. Tran, A., Hamad, W. Y. & MacLachlan, M. J. Tactoid annealing improves order in self-assembled cellulose nanocrystal films with chiral nematic structures. *Langmuir* **34**, 646–652 (2018).

Acknowledgements

Author contributions

C.H.R. did all experimental work and J.P.F.L did most fitting and statistical analysis and coordinated the writing of the paper. Both authors discussed the results and their implications, and were involved in all stages of the study as well as paper preparation.

Competing interests

The authors declare no competing interests.

Additional information

Supplementary information is available for this paper at https://doi.org/10.1038/s43246-020-00069-z.

Correspondence and requests for materials should be addressed to J.P.F.L.

Reprints and permission information is available at http://www.nature.com/reprints

Publisher's note Springer Nature remains neutral with regard to jurisdictional claims in published maps and institutional affiliations.